

Article

Influence of Various Processing Routes in Additive Manufacturing on Microstructure and Monotonic Properties of Pure Iron—A Review-like Study

Christof J. J. Torrent ^{*}, Seyed Vahid Sajadifar , Gregory Gerstein , Julia Richter  and Thomas Niendorf 

Institute of Materials Engineering, University of Kassel, 34125 Kassel, Germany; sajjadifar@uni-kassel.de (S.V.S.); gerstein@iw.uni-hannover.de (G.G.); julia.richter@uni-kassel.de (J.R.); niendorf@uni-kassel.de (T.N.)

^{*} Correspondence: torrent@uni-kassel.de

Abstract: Additive manufacturing processes have attracted broad attention in the last decades since the related freedom of design allows the manufacturing of parts with unique microstructures and unprecedented complexity in shape. Focusing on the properties of additively manufactured parts, major efforts are made to elaborate process-microstructure relationships. For instance, the inevitable thermal cycling within the process plays a significant role in microstructural evolution. Various driving forces contribute to the final grain size, boundary character, residual stress state, etc. In the present study, the properties of commercially pure iron processed on three different routes, i.e., hot rolling as a reference, electron powder bed fusion, and laser powder bed fusion, using different raw materials as well as process conditions, are compared. The manufacturing of the specimens led to five distinct microstructures, which differ significantly in terms of microstructural features and mechanical responses. Using optical and electron microscopy as well as transmission electron microscopy, the built specimens were explored in various states of a tensile test in order to reveal the microstructural evolution in the course of quasistatic loading. The grain size is found to be most influential in enhancing the material's strength. Furthermore, substructures, i.e., low-angle grain boundaries, within the grains play an important role in terms of the homogeneity of strain distribution. On the contrary, high-angle grain boundaries are found to be regions of strain localization. In summary, a holistic macro-meso-micro-nano investigation is performed to evaluate the behavior of these specific microstructures.

Keywords: pure iron; additive manufacturing; microstructural evolution; multi-scale analysis; mechanical properties



Citation: Torrent, C.J.J.; Sajadifar, S.V.; Gerstein, G.; Richter, J.; Niendorf, T. Influence of Various Processing Routes in Additive Manufacturing on Microstructure and Monotonic Properties of Pure Iron—A Review-like Study. *Metals* **2024**, *14*, 557. <https://doi.org/10.3390/met14050557>

Academic Editor: Antonello Astarita

Received: 28 March 2024

Revised: 2 May 2024

Accepted: 4 May 2024

Published: 8 May 2024



Copyright: © 2024 by the authors. Licensee MDPI, Basel, Switzerland. This article is an open access article distributed under the terms and conditions of the Creative Commons Attribution (CC BY) license (<https://creativecommons.org/licenses/by/4.0/>).

1. Introduction

In recent years, academic as well as industrial research has shown an increased interest in additive manufacturing (AM) methods. Powder bed (PB)-based processing machines are in focus due to their unprecedented design freedom [1]. In the field of PB-AM, laser-based and electron beam based powder bed fusion of metals (PBF-LB/M and PBF-EB/M, respectively) processes are the most established AM techniques. Both machine types differ mainly in the energy source used to selectively melt the raw material, i.e., the electron or the laser beam, and in some necessary built-in chamber constraints and process steps: In the PBF-EB/M process, the kinetic energy of accelerated electrons is used to melt the material. The energy delivered to the PB would rapidly decrease at ambient pressure, for which a high vacuum is required in the chamber. Due to this, powder protection is additionally given, and the pick-up of volatile elements from the atmosphere is impeded. In the PBF-LB/M process, an inert gas at ambient pressure is used to protect the material from oxidation. Apart from the atmosphere, the build chamber temperatures also differ significantly. While in the PBF-LB/M process the material can be directly melted from the powder state, the electron beam in the PBF-EB/M process would cause an electrostatic loading of the

particles, leading in turn to repulsion or *smoke* [2,3]. In consequence, every layer of the loose powder bed has to be sintered by means of a highly defocused electron beam, leading to relatively high temperatures in the build chamber. However, this high temperature level has a significant influence on the thermal gradients and, thus, solidification and (re-)crystallization behavior, respectively. On the contrary, the comparably low process temperature in the PBF-LB/M process leads to steep temperature gradients, high cooling rates, and elevated stress states. These stresses may also have a contribution to work hardening [4] and grain refinement [5], as Song et al. could find for iron. Obviously, these characteristics finally determine the mechanical and corrosive properties of the processed material, even if the powders are chemically equal.

Furthermore, a high potential for macro- and microstructural adjustments in AM, e.g., direct design of grain size, grain boundary character, and texture, is well-documented in the literature. Independently from the used energy source, possibilities to directly design the microstructure are manifold in AM and concern mainly the manipulation of temperature gradients and solidification velocity via scanning strategy [6–8], melt pool geometry and overlap [9–12], and overall build chamber temperature [8]. Furthermore, since the material is constantly re-melted and tempered in the layer-wise process, a cyclic heat treatment prevails, e.g., affecting martensitic hardening of steels [13,14], precipitation hardening [15], or grain refinement [3,16–18] during manufacturing. Apart from these interface-based hardening mechanisms, micron-scaled dislocation networks were reported in PBF-LB/M manufactured materials, e.g., austenitic stainless steel. These networks were attributed to a unique thermo-mechanical in-process treatment, eventually promoting recovery and recrystallization processes due to the heating and cooling in the layer-based process [19,20]. By means of transmission electron microscopy (TEM), Liu et al. [21] could furthermore demonstrate that these networks act as relatively weak obstacles to dislocation movements, promoting both high ductility and significant strengthening at the same time. Obviously, studies reporting on the strengthening mechanisms of metallic components can contribute to the overall understanding of the material response and are, therefore, important for providing processing guidelines to adjust structural and mechanical properties.

With respect to the mechanical performance of materials, numerous novel alloy systems have come into focus in the last few decades. High-manganese steels showing *Twinning and Transformation Induced Plasticity* (TWIP and TRIP), respectively, revolutionized the strength-ductility tradeoff in iron-based alloys [22–24]. Furthermore, *High Entropy Alloys* (HEA) were intensively studied due to their manifold deformation and strengthening mechanisms [25]. Apart from such novel alloys, the processing technologies are of highest significance since the inner structure of the materials governs their properties. A variety of *Severe Plastic Deformation* (SPD) processes can be used to achieve ultra-fine-grained (UFG) microstructures, enormously increasing the strength of the material via the Hall-Petch relationship [26]. These materials and processes are not common so far; however, they address specific applications. Still, the most common material for construction is low-alloy ferritic steel due to its wide availability, low cost, and reasonable strength. However, in the field of AM, a lack of understanding prevails when focusing on this specific material class. As mentioned above, PB-AM processing routes are gaining much interest; nevertheless, neither the processes itself nor the raw materials are characterized by a low price. The manufacturing times are relatively high, and the prior atomization of the raw material represents an additional processing step. Therefore, approaches to lower costs are highly interesting. This can be done, amongst others, by lowering the cost of the feedstock. Here, water atomization (WA) is more cost-efficient than gas atomization (GA) and is the subject of recent studies, e.g., [27]. Also, the use of wider powder size distributions and recycled powders can lower the material costs. However, powder shape and size distribution have an impact on flowability and PB density, which may influence the final part quality [28].

In the current review-like study, five different conditions of commercially pure (cp) iron are analyzed and directly compared: Two different cp-Fe feedstocks (i.e., GA and WA) processed via PBF-LB/M (cf. [27]); two conditions processed via PBF-EB/M but

using different build plate sizes (cf. [29]); as well as hot-rolled cp-Fe. These five material conditions are finally characterized by distinct structural and mechanical properties. By doing so, unique microstructures of the same material can be investigated and directly compared to comprehend micromechanical processes, regardless of the processing route. Based on quasistatic tensile tests, in situ digital image correlation (DIC), microstructural investigations in different deformation states, and TEM analysis, the mechanical response of differently processed specimens is assessed from the macro- to the nanoscale. It is shown that the global mechanical response is significantly different, and insights into the contributing elementary deformation mechanisms of cp-Fe as a model material are gained. The presented overview highlights a promising pathway toward efficient evaluation of AM-related microstructural phenomena and their related behavior upon mechanical loading.

2. Materials and Experimental Methods

2.1. Raw Material and Manufacturing

In the present study, five different Fe conditions were investigated. Further details on all materials considered are provided in previous works [27,29–32]. All conditions experienced very distinctive thermal and mechanical histories. Hot-rolled (HR) Fe-bars (ALLIED METALS CORP., Auburn Hills, MI, USA) were used as the first batch for assessment, and for powder production via electron induction gas atomization (EIGA; TLS TECHNIK BITTERFELD, Bitterfeld-Wolfen, Germany). From the GA material, two different powder size fractions were extracted. A fraction ranging from 63 to 150 μm was used as raw material on an Arcam A2X (ARCAM AB, Mölnlycke, Sweden) PBF-EB/M machine. Here, plates of different sizes, i.e., $100 \times 100 \text{ mm}^2$ and $50 \times 50 \text{ mm}^2$ (plate₁₀₀ and plate₅₀, respectively), were used. The specimens probed are named as *PBF-EB/M, plate₁₀₀ Fe* and *PBF-EB/M, plate₅₀ Fe* in the remainder of the text. Furthermore, the GA powder fraction ranging from 20 to 63 μm , as well as WA powder (HÖGANÄS AB, Höganäs, Sweden) $\leq 100 \mu\text{m}$, were processed on an SLM280 HL (SLM SOLUTIONS, Lübeck, Germany) PBF-LB/M machine. The processed specimens are named *PBF-LB/M, GA Fe*, and *PBF-LB/M, WA Fe*, respectively. For clarity, Figure 1 gives an overview of the raw materials used and the nomenclature used for the built specimens.

Both fractions of the GA powder particles provided are generally spherical, whereas the WA powder is irregularly shaped. As mentioned above, the sintering and melting parameters used to manufacture the plate₁₀₀ and plate₅₀ specimens on the PBF-EB/M machine were kept constant except for the sintering area, which was adapted to the different sizes of the build plates (cf. Table 1). In consequence, the plate₅₀ process resulted in a higher chamber temperature than the plate₁₀₀ process, which is traced back to a differing behavior of heat flow. It was shown that these differences lead to different microstructural and mechanical properties [29]. Furthermore, for the sake of direct comparison, the GA powder as well as the WA powder were processed using the same PBF-LB/M parameters [27].

Table 1. Parameters applied on both machines to process the different Fe powder materials. A layer thickness of 50 μm was used for both machines.

Arcam A2X	Preheat	Melt	SLM 280 HL	Melt
	I = 15 mA	I = 12.25 mA		P = 300 W
	v = 12.000 mm/s	v = 4.000 mm/s		v = 800 mm/s
	12 repetitions	hatch = 0.08 mm		hatch = 0.1 mm

In PB-AM, several factors can highly impact the material's final appearance, as will be discussed in this work. For instance, the beam parameters used to insert the energy necessary for melting can vary the local heat flow and thus the solidification and recrystallization processes in a wide range. In previous, not-published studies, different hatches, beam speeds, beam powers, and preheat parameters (in the case of PBF-EB/M) have been regarded, investigating their impact on relative density, texture, and grain size. For the ma-

material conditions presented herein, elaborated parameter sets ensuring the highest relative densities have been applied. An overview of the process parameters applied to manufacture the specimens is given in Table 1. Applying these, cuboids of $10 \times 10 \times 40 \text{ mm}^3$ have been built directly on the build plates, i.e., without any support structures, with the longest axis parallel to the build direction (BD).

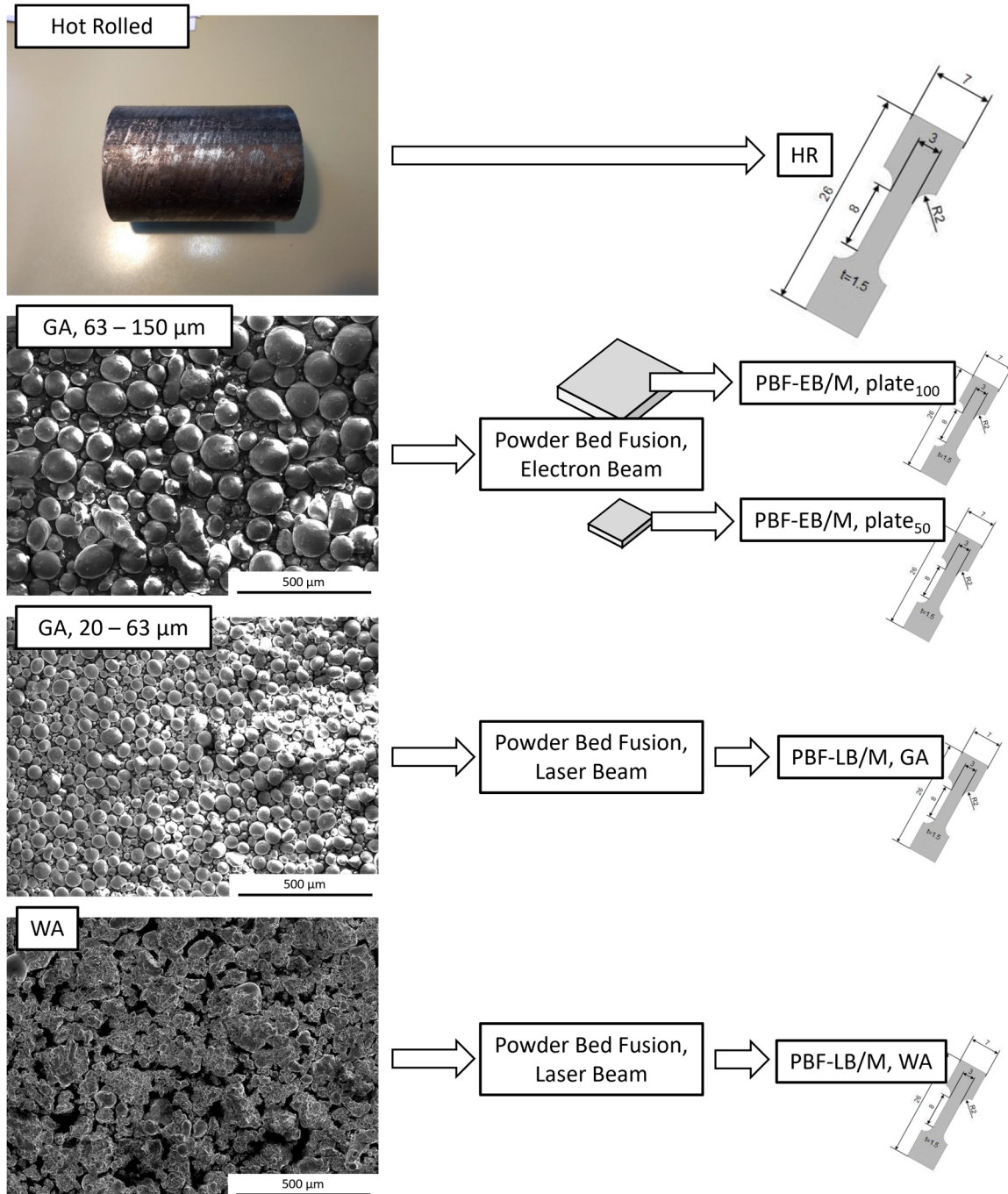


Figure 1. Schematic showing the raw materials (left column), the machines used to process these materials (middle column) and the resulting specimens built and machined, which are finally used for assessment.

The chemical composition of the as-processed Fe specimens (cf. Table 2) was analyzed by REVIERLABOR GMBH (Essen, Germany). The analysis was performed using X-ray fluorescence for metallic elements, carrier gas hot extraction for hydrogen, nitrogen, and

oxygen, and combustion analysis for carbon and sulfur. As can be seen in Table 2, the purity levels of the five material conditions slightly vary. Especially the specimen built from WA powder shows an increased fraction of Cr, Cu, Mn, and Ni, stemming probably from the initial batch used for production. Other impurities and interstitial elements are at a similar level for all conditions, still showing the highest values of O and N for PBF-EB/M, plate₅₀ and the lowest for PBF-EB/M, plate₁₀₀.

Table 2. Chemical composition of the five Fe conditions considered in present work (partly recompiled from [27,30]).

Element	HR	PBF-EB/M, plate ₁₀₀	PBF-EB/M, plate ₅₀	PBF-LB/M, GA	PBF-LB/M, WA
Al	0.008	0.005	<0.005	<0.02	<0.02
Cr	<0.01	<0.01	<0.01	<0.02	0.14
Cu	<0.01	0.01	0.01	<0.02	0.03
Fe	Basis	Basis	Basis	Basis	Basis
Mn	0.03	0.03	<0.01	0.04	0.09
Ni	<0.01	0.01	0.02	0.04	0.07
O	0.0166	0.0059	0.017	0.016	0.020
N	0.005	<0.002	0.018	0.008	0.003
C	<0.005	<0.005	<0.005	<0.005	<0.005

2.2. Mechanical Testing

All specimens considered were cut via electrical discharge machining (EDM) out of the HR bars as well as the built cuboids, with the load axis parallel to the rolling direction, or BD, respectively. All microstructural as well as mechanical investigations presented in the following sections have then been performed in the middle of the extracted specimens, hence around 20 mm away from both the build plate and the last layer to ensure the information is not influenced by related phenomena. The specimens were then ground to a surface roughness of μm , and one side of each specimen was further polished to $0.05 \mu\text{m}$ for the microstructural investigations described below. For characterization of the active deformation mechanisms under quasistatic mechanical loading, two specimens per condition were subjected to tensile tests using an in-situ tensile rig (KAMMRATH & WEISS GmbH, Schwerte, Germany) operated in displacement control at a speed of $5 \mu\text{m s}^{-1}$. The nominal cross section of the specimens was 4.5 mm^2 ; however, in every test, the actual cross section of the specimen was determined and used for stress calculation. Since the testing setup does not allow for recording the strain via an extensometer, the crosshead displacement was used for strain calculation. The HR specimens were loaded in a rolling direction, and the AM specimens were manufactured in BD, respectively. For every condition, one specimen was tested to a crosshead displacement of $820 \mu\text{m}$, which equals a nominal strain of 10.25%. During the tests, the elongation was interrupted in increments of 0.5% up to 5%, and increments of 0.75% up to 10.75% to capture micrographs of the specimen surface. Upon reaching 10.25% strain, the tensile test was stopped and the specimen was unloaded. All in situ micrographs were captured within the same area, i.e., the area of the microstructural measurements before and after tensile testing (see next paragraph). Due to the testing procedure applied a serrated course of tensile curves is seen. For a conclusive evaluation, one specimen per condition was tested up to failure to obtain the entire stress-strain information. It is well known that, due to possible microstructural anisotropy, the material resistance may be dependent on the direction of loading with respect to BD. So, for example, elasticity, plastic deformation, and crack growth may correlate with texture and the number of grain boundaries orthogonal to the load axis (inter alia). In this work, specimens have only been loaded parallel to BD.

2.3. Microstructural Investigation

For the interrupted tensile tests, fine SiC particles were sprayed onto the specimens to create an adequate speckle pattern. From this pattern, the DIC software is able to calculate local strains on the specimen surface. During the tensile tests, optical micrographs were captured using a Keyence VHX-600 (KEYENCE, Neu-Isenburg, Germany) digital optical microscope and a VH Z100 objective. Afterwards, the images were processed using DIC software VIC-2D, version 6 (CORRELATED SOLUTIONS, Irmo, SC, USA). For best correlation results, evaluation parameters, i.e., the subset size, had to be adapted in a range of 20 to 45 pixels at a constant step size of 2 pixels. After correlation, an evaluation was performed considering Lagrange displacement in the load direction. Due to visual changes to the applied spackle pattern, correlations at very high magnitudes were not feasible; thus, a reliable, more detailed view of strain distribution at higher magnitudes is not possible.

On the same specimens, microstructural investigations were performed in the as-built condition and after 10.25% elongation using a scanning electron microscope (SEM, TESCAN CAMSCAN MV 2300, Brno, Czech Republic) equipped with an electron backscatter diffraction (EBSD) detector. Data were evaluated using TSL OIM software, version 7 (EDAX, Mahwah, NJ, USA). A strain of 10.25% is still in the regime of uniform elongation for all considered conditions. Thus, it can be assumed that the information gained via the methods applied is representative of the whole specimen. The DIC and EBSD measurements were performed on the same spots in order to provide insights into the micro- and macroscale grain structure evolution. A relatively low magnification was chosen for the EBSD measurements. To assess the structural evolution within the same specimen volumes, the surfaces were only cleaned and not polished for the EBSD measurement after the 10.25% tensile test. Therefore, the surfaces are characterized by a significant change in topography, as highlighted in Figure 2.

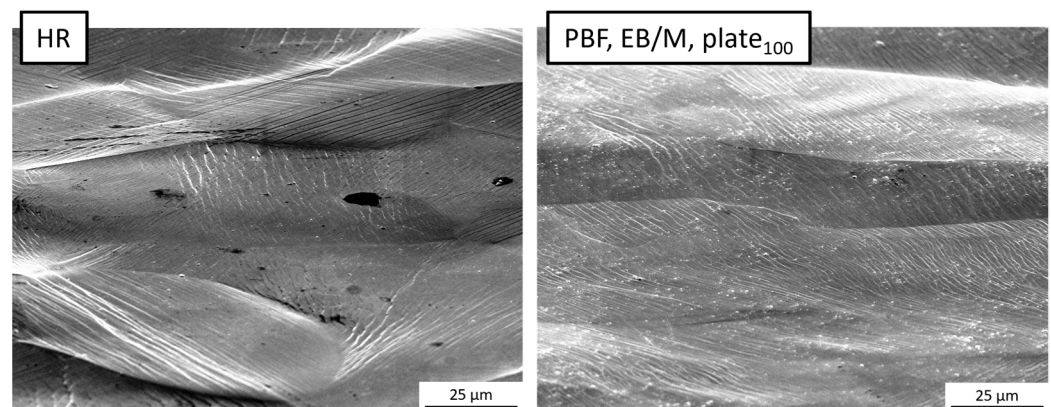


Figure 2. Representative images of the HR and PBF-EB/M, plate₁₀₀ specimen surfaces after being subjected to a nominal strain of 10.25%.

Due to these two reasons, i.e., large surface areas probed and low surface quality in the case of the strained specimens, the image quality (IQ) is not constantly high on the whole surface. The inverse pole figure (IPF) maps given in the present work are cropped to show the same specimen region before and after testing, while kernel average misorientation (KAM) maps are chosen only from the regions being characterized by the highest IQ and can only be taken into consideration for qualitative comparison. In any case, the SEM was operated at a nominal voltage of 30 kV, and the step sizes have been adapted to the level of magnification, i.e., 2 μm, 0.75 μm, and 0.5 μm for 150×, 800×, and 2000×, respectively. For KAM evaluation, the misorientation angles between a pixel and its first nearest neighbor were considered in a range from 0° to 5°. Here, KAM maps are only considered with the objective of qualitatively detecting dislocation concentrations and are not used for quantification of the latter.

Subsequently, disc-shaped specimens with a diameter of 3 mm were cut via EDM from the gauge length of the specimens strained to nominally 10.25% for TEM analysis. The discs were mechanically thinned to 60 μm and electropolished with an electrolyte consisting of 160 mL perchloric acid, 380 mL butoxyethanol, and 460 mL acetic acid in a TenuPol-5 Jet polishing system (STRUERS, Willich, Germany). The investigations were performed on a CM200 TEM (PHILIPS, Amsterdam, The Netherlands) equipped with a LaB6 source and operated at an accelerating voltage of 200 kV. Finally, the fracture surfaces of the specimens strained until failure were characterized using the SEM mentioned above, operated at a nominal voltage of 20 kV. For postmortem characterization, the specimens were ground and polished again and analyzed by means of EBSD in these regions. As already mentioned before, the material conditions regarded herein have already been investigated in other studies; thus, the authors refer to [27,29–32] for further manufacturing data and material characteristics.

3. Results and discussion

3.1. In Situ Tensile Test

Figure 3 displays the interrupted tensile tests conducted for in situ imaging. Due to the interruptions, the courses of the curves are obviously affected by a localized stress decrease. Here, the Hook's Straight can be seen upon unloading being parallel for every specimen. For the testes conducted, this line is representative of the elastic behavior of the entire system, composed of the specimen and stress rig.

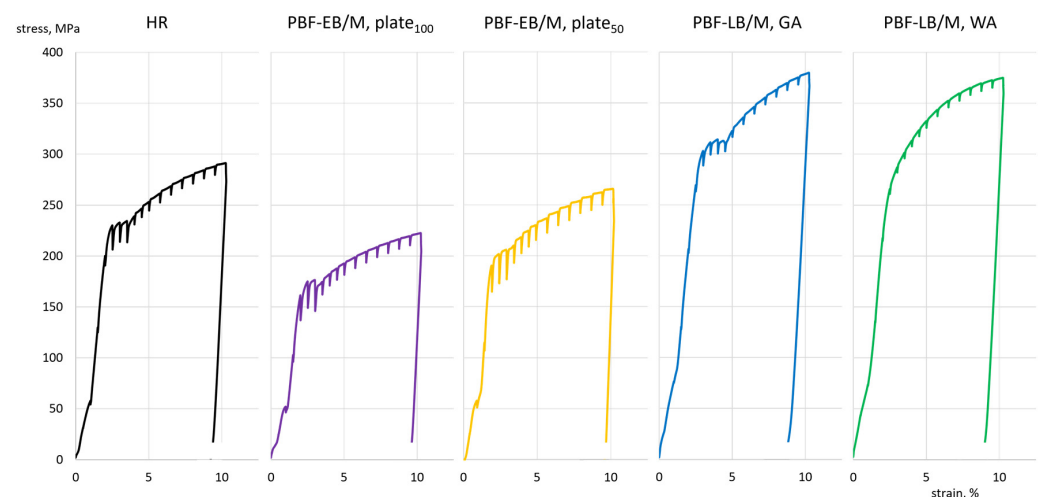


Figure 3. Interrupted tensile tests of the five compared Fe conditions. The differences in YS are obvious, furthermore a pronounced yield phenomenon can be seen in all conditions except for the PBF-LB/M, WA specimen.

The differences in yield strength (YS) of the five conditions are obvious. Here, the two PBF-EB/M manufactured specimens show the lowest values, followed by the HR specimen and the two PBF-LB/M specimens with the highest YS. A pronounced yield phenomenon can be seen in most cases, but, not in the PBF-LB/M, WA specimen. This phenomenon is usually attributed to the presence of interstitials pinning dislocations at the onset of plastic deformation. The specimen built from WA raw material shows the highest level of substitutional atoms, particularly Cr, Cu, and Mn (cf. Table 2). Interstitials being present, i.e., O and N, can be expected to form oxides and nitrides, which in turn are known to promote precipitation hardening; however, at the same time, they decrease sensitivity toward strain aging phenomena. The highest purity was measured for the PBF-EB/M, plate₁₀₀ specimen. This material shows the lowest YS, inter alia, due to a lack of strengthening by impurities. Still, other factors could be involved, which will be investigated in the remainder of this work.

Selected DIC images used to analyze the homogeneity of deformation are presented in Figure 4, in which the global strain (taken from the stress rig) for every specimen increases in the columns from left to right. As is visible from the HR specimen in the upper row, correlations are less clear and voids appear at strains higher than 4%, which can be traced back to the evolution of a strong surface topography as well as harsh strain gradients.

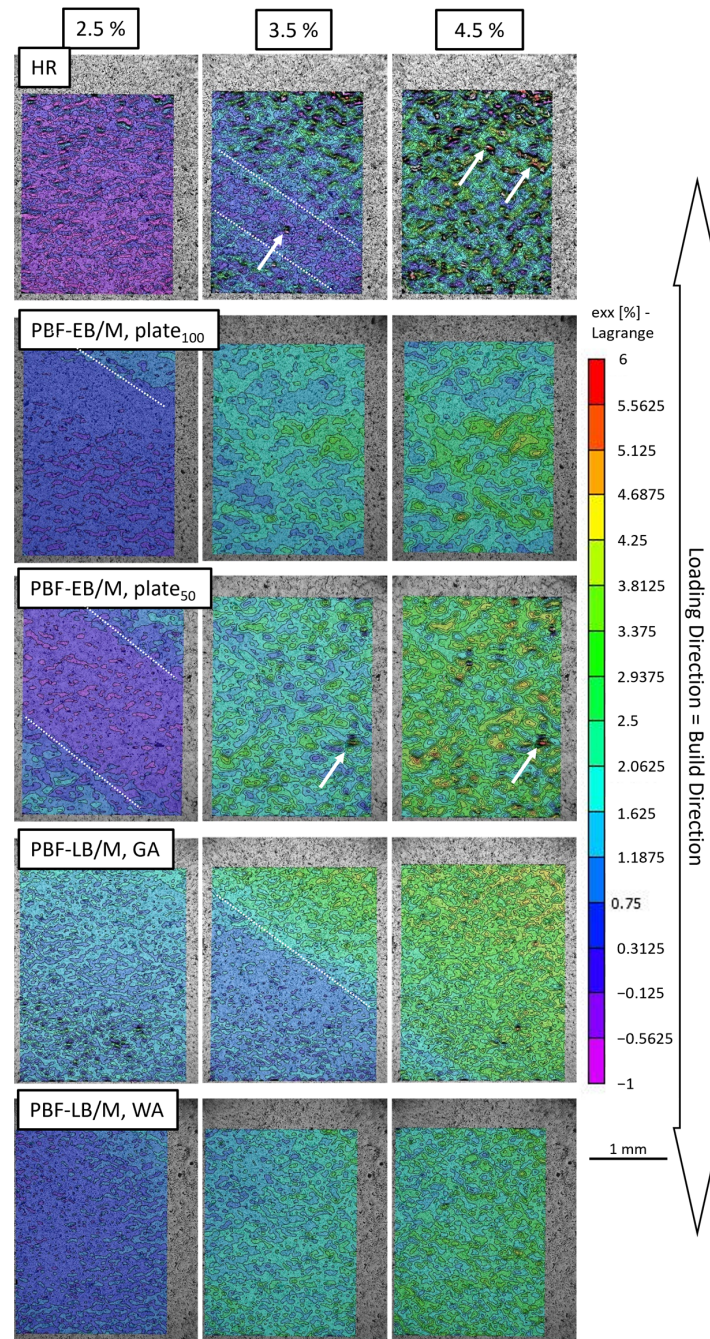


Figure 4. DIC results of the five Fe conditions. The global deformation increases from left to right. Lüders bands (dotted lines) become visible in all but the PBF-LB/M, WA Fe specimen. Already at a global strain of 3.5%, the HR and the PBF-EB/M, plate₅₀ specimen locally show poor correlation (white arrows), while a predominantly homogeneous strain distribution dominates both PBF-LB/M specimens. Images are taken at a magnification of 100x, strains indexed are in loading direction. As visualized by the double arrow on the right hand-side, the loading direction is parallel to the build direction. Note: for HR Fe the build direction is not applicable, here loading direction is equal to rolling direction.

The images taken at 2.5% correspond to strain states at the onset of plastic deformation, and the images taken at 3.5% are located in the region where the most pronounced yield phenomena are seen for most specimens (Figure 3). In all specimens but the PBF-LB/M, WA, Lüders band formation is evident in the DIC images (Figure 4), reflecting bands at an angle of about 50° to the loading direction. As for the absence of a pronounced YS, the absence of Lüders bands in PBF-LB/M, WA, can be attributed to the formation of oxides and nitrides. The PBF-EB/M, plate₁₀₀ and both PBF-LB/M specimens show a homogeneous deformation up to 4.5% strain, while the HR and PBF-EB/M, plate₅₀ specimens are characterized by strain localizations already at 3.5% strain, evident through sharp gradients in color coding (cf. white arrows). As a consequence, higher strains and, hence, more severe localizations can be responsible for poor DIC correlations at these sites. Among others, the character of strain and stress distributions within the material can be attributed to the homogeneity of the matrix, grain size, and grain boundary character, as elaborated in the following section.

3.2. Microstructural Evolution

The microstructures of the five Fe specimens are shown in Figure 5. Already before loading, the structures differ significantly in terms of grain size, shape, and boundary character. HR-Fe is characterized by an equiaxed grain morphology featuring mainly high-angle grain boundaries (HAGBs). The latter are defined by a misorientation angle > 15° and black lines in Figure 5, while low-angle grain boundaries (LAGBs) with misorientations ranging from 2° to 15° are indicated by white lines. Furthermore, the IPF map shows uniform color coding at every grain point with only low deviations within a grain, indicating a normalizing or recovery heat treatment following the HR process. However, no information on the thermo-mechanical history of the HR material could be provided by Allied Metals. After applying the strain, minor changes within the grains are visible. Similar to the HR condition, the PBF-EB/M plate₅₀ Fe is characterized by an equiaxed structure, and also here minor changes become visible upon straining.

Significant plastic deformation and dislocation activity already can be seen in the as-built, undeformed PBF-EB/M plate₁₀₀ specimen through obvious color variations within the grains, which increased upon deformation. Despite a different grain size, the PBF-LB/M, WA, and GA specimens are characterized by a similar appearance, showing slightly elongated grains in BD and featuring LAGBs and obvious mosaicity before and after loading.

The grain sizes of the five Fe conditions in the as-built state were determined by OIM software based on the diameter of circles with the same area as the grains and are displayed in Table 3. For the two PBF-LB/M manufactured specimens, a lower grain size compared to the HR and both PBF-EB/M specimens is obvious, whereby the GA raw material led to smaller grains than the WA. The relationship between grain sizes and YS values is in good correlation with the Hall-Petch theory.

The grain structure formation of additively manufactured specimens is heavily influenced by the overall process temperature. The PBF-EB/M process is characterized by high process temperatures, lower cooling rates, and, therefore, a very low residual stress state compared to the PBF-LB/M process. Both processes share a common characteristic of repetitive energy input from the following layers, i.e., while the latest layers are only melted, reheating of the underlying, already solidified layers occurs. Depending on the global temperature level, this rapid cooling and reheating leads to a different number of $\alpha \leftrightarrow \gamma$ phase transformations, eventually having a strong impact on grain refinement. The characteristic temperature path plays a significant role in the structural evolution of materials showing allotropic phase transformations and was already described in [3,7,11,16,18]. In this regard, a significant change in grain sizes could be observed using the same manufacturing process, but there could be a higher or lower number of phase transformations in consequence of the thermal history [29,31]: The PBF-EB/M, plate₅₀ Fe experienced higher processing temperatures, allowing for a refinement of previously solidified grains, while a slightly lower process temperature in the PBF-EB/M, plate₁₀₀ process lead to a recovery rather than

recrystallization and, therefore, to the formation of a high fraction of LAGBs (white lines in Figure 5) rather than HAGBs.

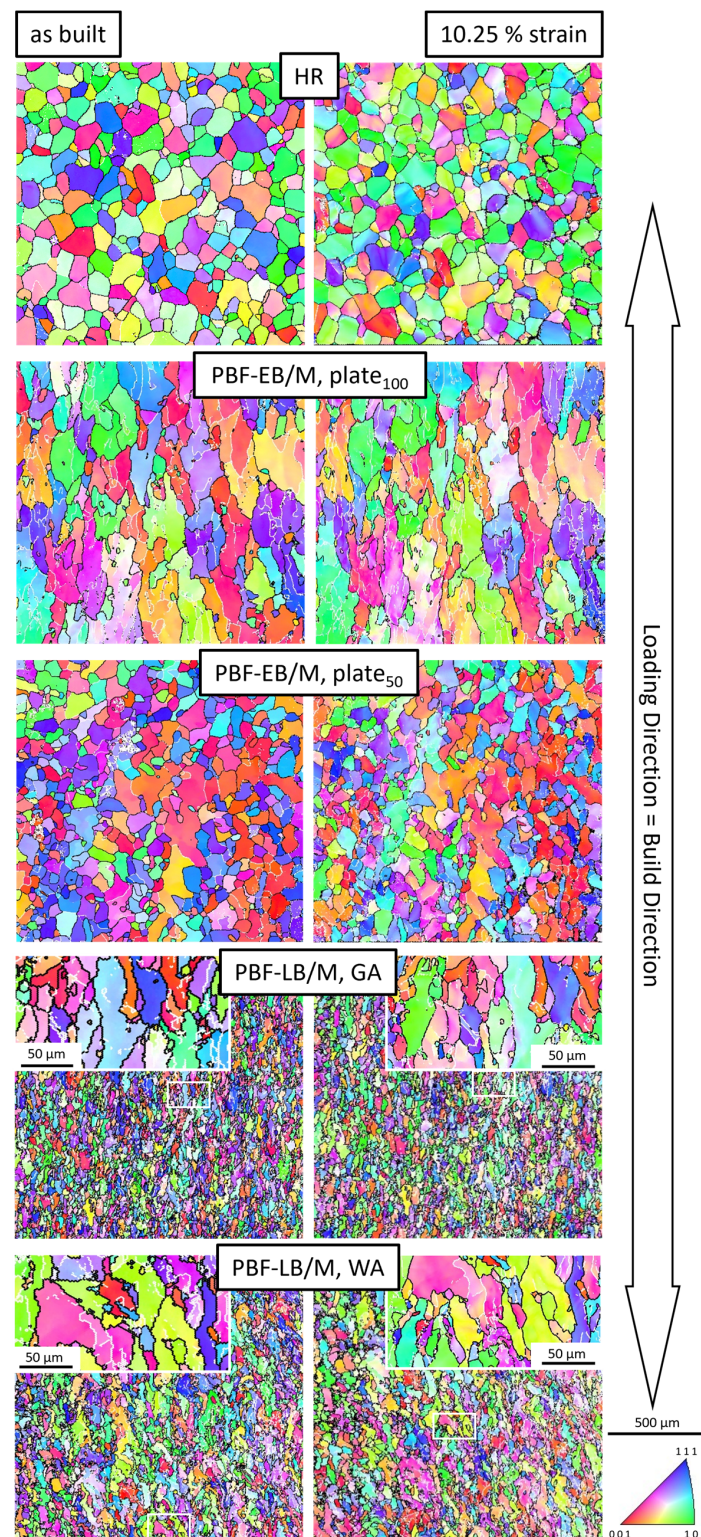


Figure 5. IPF maps for the five compared specimens, indexed with respect to the vertical, i.e., loading direction, with marked grain boundaries for misorientation angles from 2° to 15° in white and $>15^\circ$ in black. The left and the right column show the as-built conditions and the same area after 10.25% into strain, respectively. Note: for HR Fe the build direction is not applicable, here loading direction is equal to rolling direction.

Table 3. Grain sizes given in μm for the five Fe specimens considered, determined from OIM software.

HR	PBF-EB/M, plate ₁₀₀	PBF-EB/M, plate ₅₀	PBF-LB/M, GA	PBF-LB/M, WA
106	322	164	43	67

The above-detailed intrinsic heat treatment is very similar to the PBF-LB/M process, but here the surrounding powder bed is relatively cold. Thus, in the PBF-LB/M process, steep temperature gradients can lead to significantly higher residual stress states [33]. Eventually, this provides for a mechanical driving force, further promoting recovery and recrystallization [5,19,20]. Finally, both PBF-LB/M-manufactured Fe conditions considered in the present work show a high fraction of LAGBs and a small grain size (cf. Table 3). In PBF-LB/M, the interaction of the energy source with the material is complex and, among others, dependent on the surface appearance and relative density of the powder material used. In the case of GA and WA Fe regarded herein, differences in grain sizes are traced back to slightly differing chemical composition as well as particle morphology, which are responsible for different effective energy inputs and affecting local thermal levels and melt pool dynamics [27]. Furthermore, stresses may be reduced via dislocation movement during PBF-LB/M processing, i.e., in-process work hardening can take place [17]. Thus, a superimposition of both low grain size and work hardening provides for the high strength of the PBF-LB/M manufactured Fe specimens. For further information on the microstructural evolution of the four different PB-AM manufactured specimens, the authors refer to [27,29,30], since the present study primarily focuses on the assessment of the deformation behavior of the material conditions presented.

KAM maps of differently processed Fe specimens at strain values of 0% and 10.25% are shown in Figure 6, providing qualitative data on the evolution of dislocation density and strain localization [34]. Here, it is important to note that the shown KAM maps were obtained on specimens that have not been additionally polished after deformation (see details in the experimental section). Regardless of the processing history, an increase in strain results in a change of the KAM maps in all specimens, eventually indicating an activation of dislocation sources (e.g., Frank-Read dislocation sources), increasing the overall dislocation density to assist plastic deformation [35–37].

Before loading, no pronounced dislocation accumulation is visible in the HR as well as in both PBF-EB/M conditions. As mentioned above, this can be rationalized by a normalizing heat treatment conducted after the actual hot rolling process in the case of the HR specimens. For the PBF-EB/M specimens, the relatively low dislocation density can be traced back to the elevated temperatures during processing [38,39]. After straining, an obvious accumulation of dislocations can be seen at grain boundaries. These are especially visible in the HR as well as in the PBF-EB/M, plate₅₀ specimens. Grain boundaries are obstacles to dislocation motion, and, hence, dislocations can be piled up here [40]. The KAM maps captured at higher magnifications with lower step sizes underline these results. In contrast, in the 10.25% strained PBF-EB/M, plate₁₀₀ specimen, pile-ups at grain boundaries are not as prominent. Instead, the values seen in the KAM maps are moderate (green), pointing at the high importance of LAGBs being present within the grains. Taking into account the different boundary angles and their contribution to Hall-Petch strengthening, at the same nominal strain, the PBF-EB/M, plate₁₀₀ specimen tends to distribute internal strains and stresses more homogeneously, resulting in less pronounced strain localization at grain boundaries. This finding is in line with the above detailed DIC results (Figure 4), in which no remarkable strain concentrations could be found in this material condition.

With regard to both PBF-LB/M manufactured specimens, in-process work hardening can be deduced from the KAM maps already before loading (the maps being mostly colored green in this case). Thus, the as-built states already differ significantly from the HR and PBF-EB/M manufactured specimens in terms of initial dislocation density, aligning with previous studies on PBF-LB/M processed iron [41]. Considering the processing history, higher thermal gradients promote higher residual stress [19,38], triggering the

generation of dislocations to a greater extent compared to the PBF-EB/M process. Thus, in-process dislocation generation impacts PBF-LB/M manufactured parts significantly [42,43]. Furthermore, similar to the PBF-EB/M, plate₁₀₀ Fe, KAM maps indicate higher dislocation densities in the grain interior rather than at grain boundaries after deformation, pointing at grain internal barriers for dislocation movement.

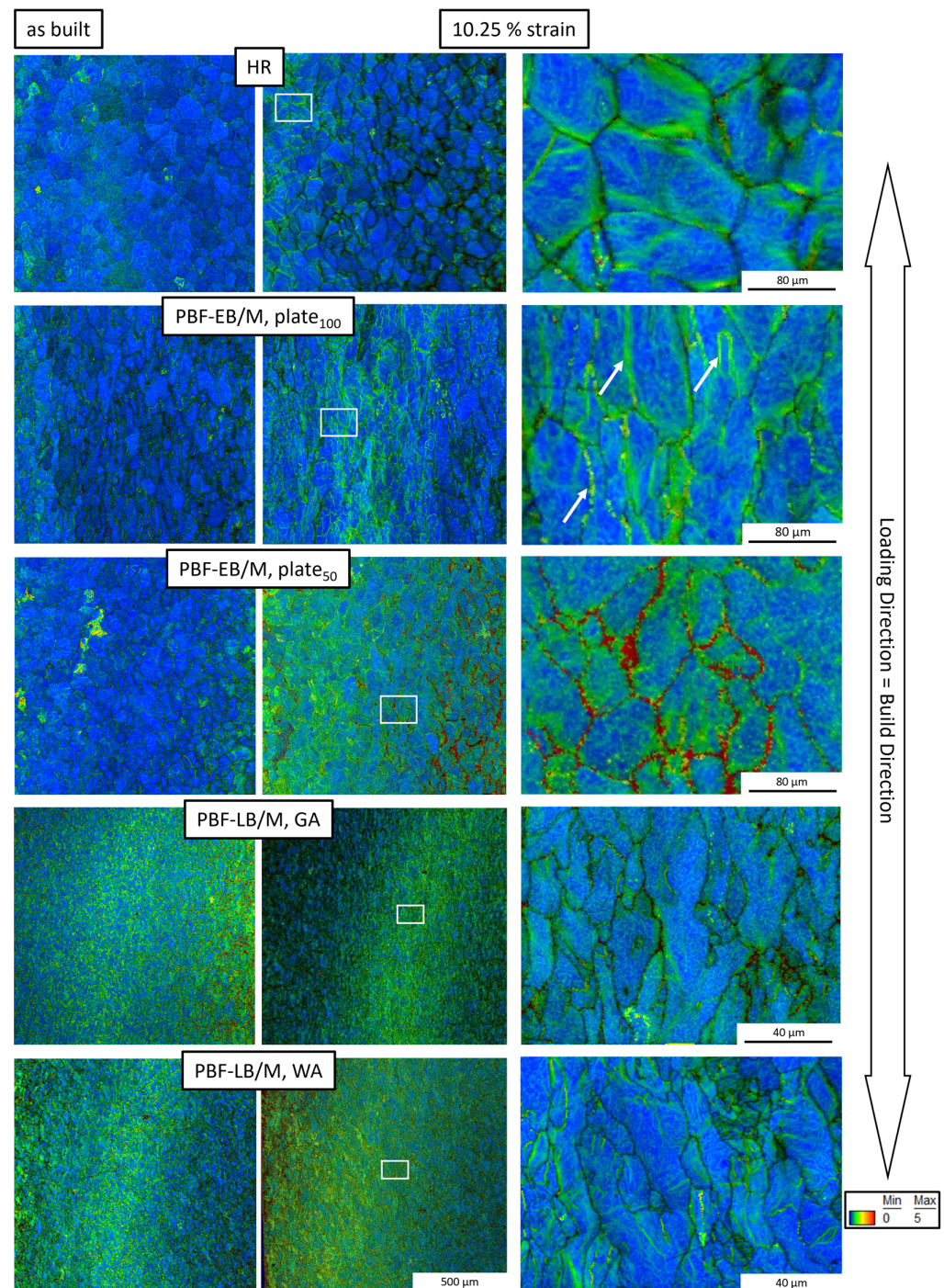


Figure 6. KAM maps of the five Fe conditions before (**left column**) and after tensile test up to 10.25% (**middle and right column**). The maps in the right column represent magnified views of the white squares in the middle column. The image quality map is superimposed, thus, the grain boundaries can be seen from the dark lines, especially at higher magnifications. White arrows pinpoint dislocation accumulation at LAGBs in the PBF-EB/M, plate₁₀₀ specimen. See text for further details. Note: for HR Fe the build direction is not applicable, here loading direction is equal to rolling direction.

Finally, it must be mentioned that the microstructural evolution of PB-AM routes is highly dependent on process parameters and their complex interplay. These parameters are not only hatch spacing, beam speed, and intensity but bear a very wide range in adjusting the energy input into the raw material and hence in the melt flow as well as solidification and recrystallization processes. However, these interrelations are difficult to observe, not yet fully understood, and are not within the scope of the presented work. Rather, the material's mechanical behavior in dependence of the microstructural architecture shall be investigated at different scales.

3.3. Complete Tensile Test

Stress-strain curves of the specimens tested up to failure are shown in Figure 7. Specimens built on the same machine applying constant parameters (i.e., PBF-EB/M, plate₁₀₀ vs. plate₅₀) can differ by about 15% in terms of UTS, and material from the same provider processed on different PB-AM routes (i.e., PBF-LB/M, GA vs. PBF-EB/M, plate₁₀₀) shows up to about 60% difference in UTS, highlighting the pronounced impact of specific processing conditions on microstructure and mechanical properties.

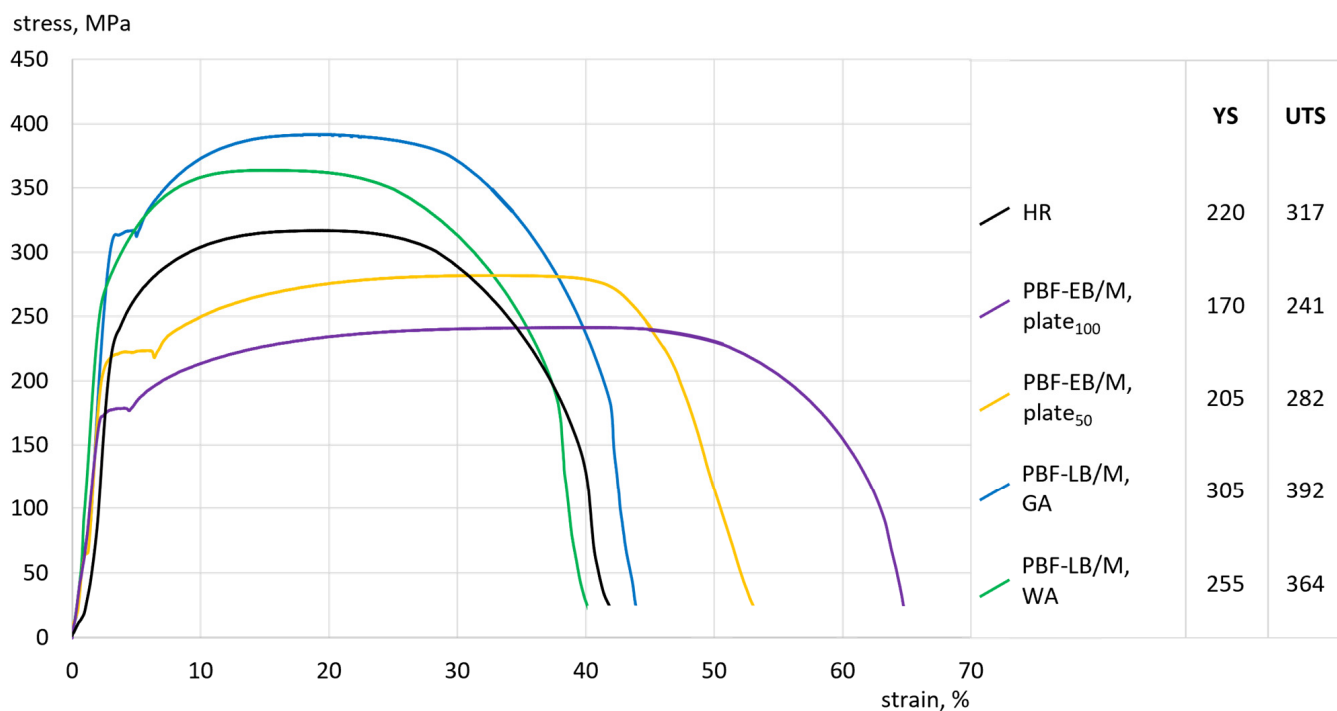


Figure 7. Tensile test conducted up to failure of the five compared Fe conditions and corresponding values for YS and UTS.

In the probed different conditions of cp-Fe (characterized by the chemical compositions listed in Table 2), strengthening mechanisms well-known for steels, i.e., martensitic hardening and precipitation hardening, are hardly to be expected. Based on an assessment of the stress-strain courses (in light of the IPF and KAM maps (Figures 5 and 6)), the activation of other elementary mechanisms can be derived. The smallest grain sizes can be found in the PBF-LB/M manufactured specimens (cf. Table 3), highly contributing to the strength of these specimens. Furthermore, KAM maps revealed a high density of dislocations already present before loading. Both aspects contribute to the material states with the highest YS.

The PBF-EB/M, plate₁₀₀ condition shows the lowest UTS and highest fracture strain. Further, a higher uniform elongation can be seen in comparison to the HR or PBF-LB/M manufactured counterparts, i.e., necking occurs only at elevated strains. After 10.25% strain, no pronounced dislocation pile-ups are visible at grain boundaries (cf. Figure 6), in contrast to the HR or PBF-EB/M, plate₅₀ conditions. Instead, dislocation arrangements can be seen inside the grains. Thus, a higher degree of plastic deformation of the PBF-EB/M, plate₁₀₀ can be explained by a more uniform strain distribution inside the material. Thus, a superior damage tolerance is characteristic of this material condition, which could further be observed in high-cycle fatigue loading [30,32,44].

In contrast, in HR and PBF-EB/M-Fe, plate₅₀ Fe strain and stress localization can be clearly seen at HAGBs. Being characterized by a similar inner grain structure and boundary character, both specimens finally show a similar YS. Still, the HR specimen shows a higher UTS, which can be traced back to the presence of aluminum oxides in the matrix (cf. Table 2) and lower grain size.

Figure 8 shows the fracture surfaces of the five specimens tested to failure. The PBF-EB/M, plate₁₀₀ specimen shows the highest degree of post-necking deformation, which is in line with the highest ductility of this material condition (cf. Figure 7). While the HR specimen displays a homogeneous fracture surface, all PB-AM specimens are characterized by larger dimples, most probably stemming from process-induced pores. Still, no unmolten particles can be seen. Despite the fact that PBF-EB/M as well as PBF-LB/M manufactured specimens are characterized by very high relative densities of >99.9% (probed via computed tomography, cf. [29,30] and [27], respectively, not shown here), defects such as lack of fusion are possible, which may enlarge to severe voids during tensile testing. The white circle in Figure 8 points at a region with insufficient layer bonding, and grain boundaries can be seen. Nevertheless, with respect to the high fracture strains of all considered specimens, these defects do not appear to be detrimental.

Finally, Figure 9 shows the microstructural changes at the region of failure investigated using EBSD. Irrespective of the processing condition, previously equiaxed as well as elongated grains are deformed along the direction of loading after tensile deformation. From the KAM maps after 10.25% strain and after failure (Figures 6 and 9; polished after failure; see experimental section for details), a dislocation multiplication due to tensile deformation becomes obvious. As pointed out above, the activation of dislocation sources contributes to dislocation generation. Cold deformation can promote the transformation of equiaxed grains into elongated ones, and grain boundary-mediated plasticity can result in stress-assisted grain growth because of the migration, rotation, and coalescence of the grains in a preferred direction for accommodating the strain paths [45,46]. Besides, the formation of slip bands in the grains is evident, eventually revealing the localization of plastic deformation [47]. Again, the LAGB-dominated material conditions are different in comparison to the HR and the PBF-EB/M, plate₅₀ Fe, the latter showing a drastically reduced image quality. This fact indicates a very high activity of dislocations, eventually promoted by the absence of LAGBs. However, lattice defect phenomena are critical to be finally evaluated by means of EBSD only and must therefore be further supported by high-resolution techniques.

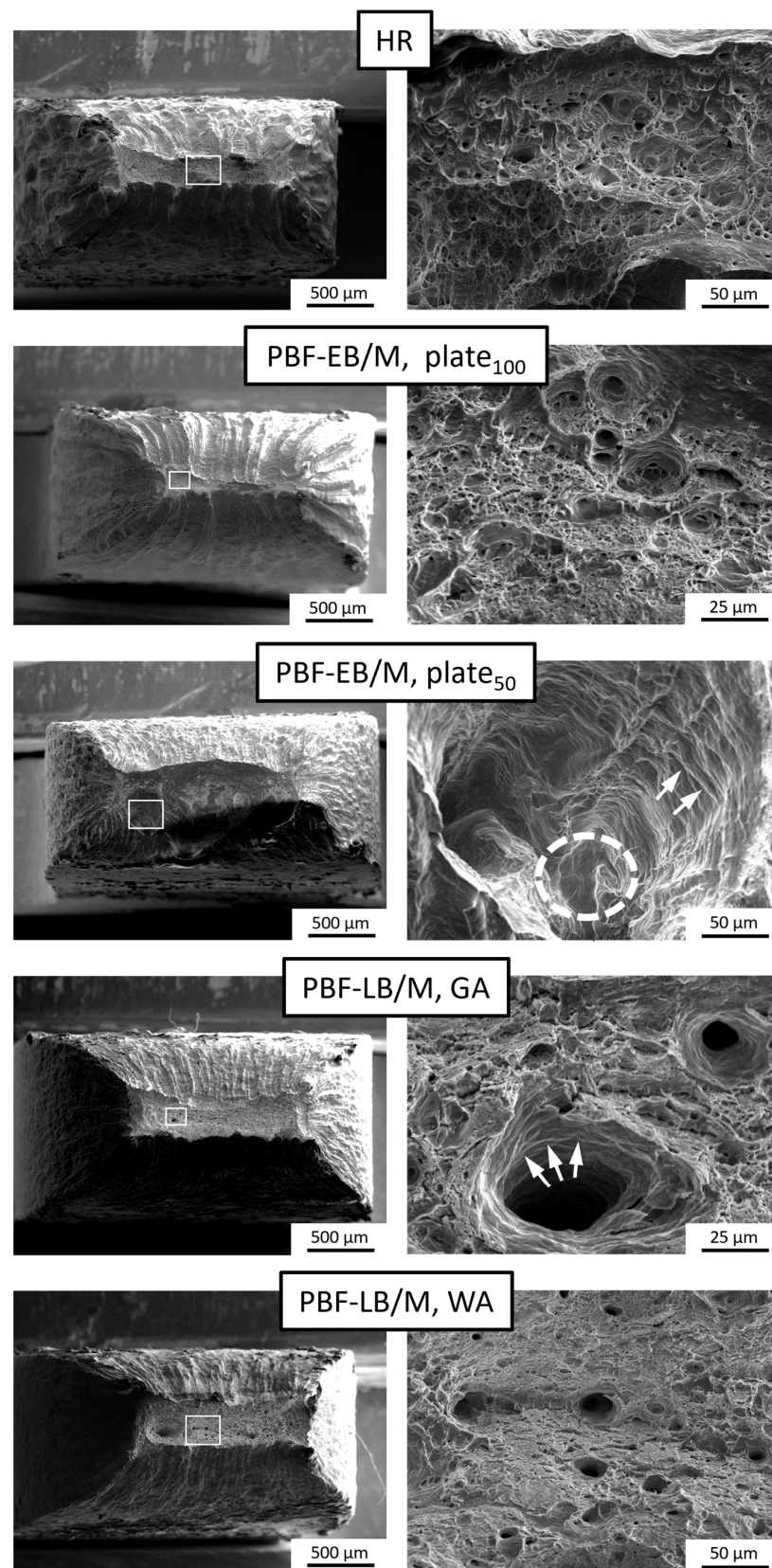


Figure 8. Fracture surfaces of the five Fe conditions after the completed tensile test. The white rectangles in the (left column) show the origin of the figures taken with higher magnification (right column). In the PBF-EB/M, plate₅₀ sample an area of lack of fusion is visible at the bottom of a void (white circle). In larger voids, slip marks are visible (white arrows).

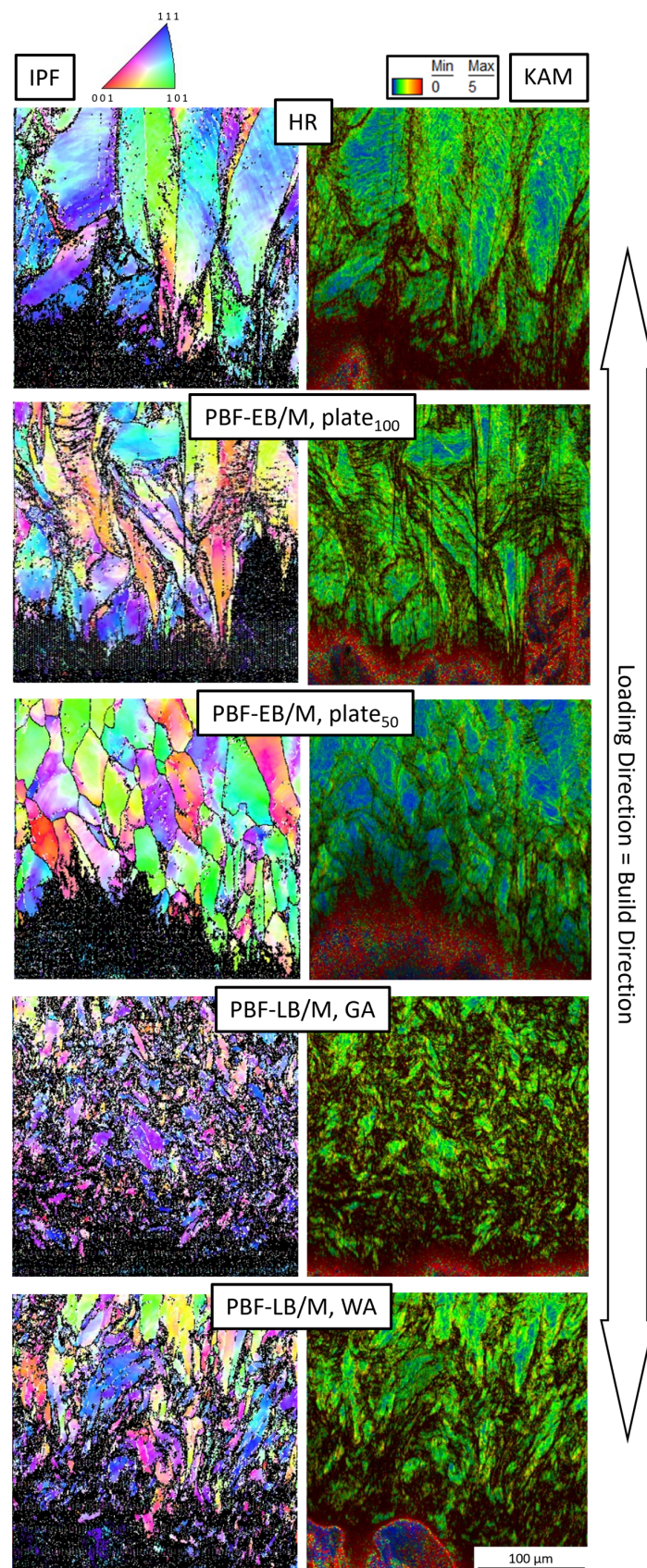


Figure 9. EBSD measurements at the crack tips of the five Fe specimens tested to failure. IPF maps indexed with respect to loading direction and KAM maps (left and right row, respectively). Note: for HR Fe the build direction is not applicable, here loading direction is equal to rolling direction.

3.4. Process-Microstructure-Property-Relationships

To shed light on the elementary processes contributing to the microstructure evolution in the condition typically being subjected to loadings in application, i.e., before necking and fracture, bright-field TEM images of differently processed Fe specimens were recorded to provide a deeper insight after a nominal deformation to a strain level of 10.25% (Figure 10). The focus is only on the three microstructures being selected based on the EBSD analysis: With a very similar structure, HR Fe is considered to be representative for the PBF-EB/M, plate₅₀ Fe as well. PBF-EB/M, plate₁₀₀ Fe is characterized by a large grain size and a high fraction of LAGBs. The latter holds true for both PBF-LB/M manufactured material conditions; however, these are characterized by a lower grain size and a higher initial stress level. Here, the GA material is considered to be representative for both PBF-LB/M conditions.

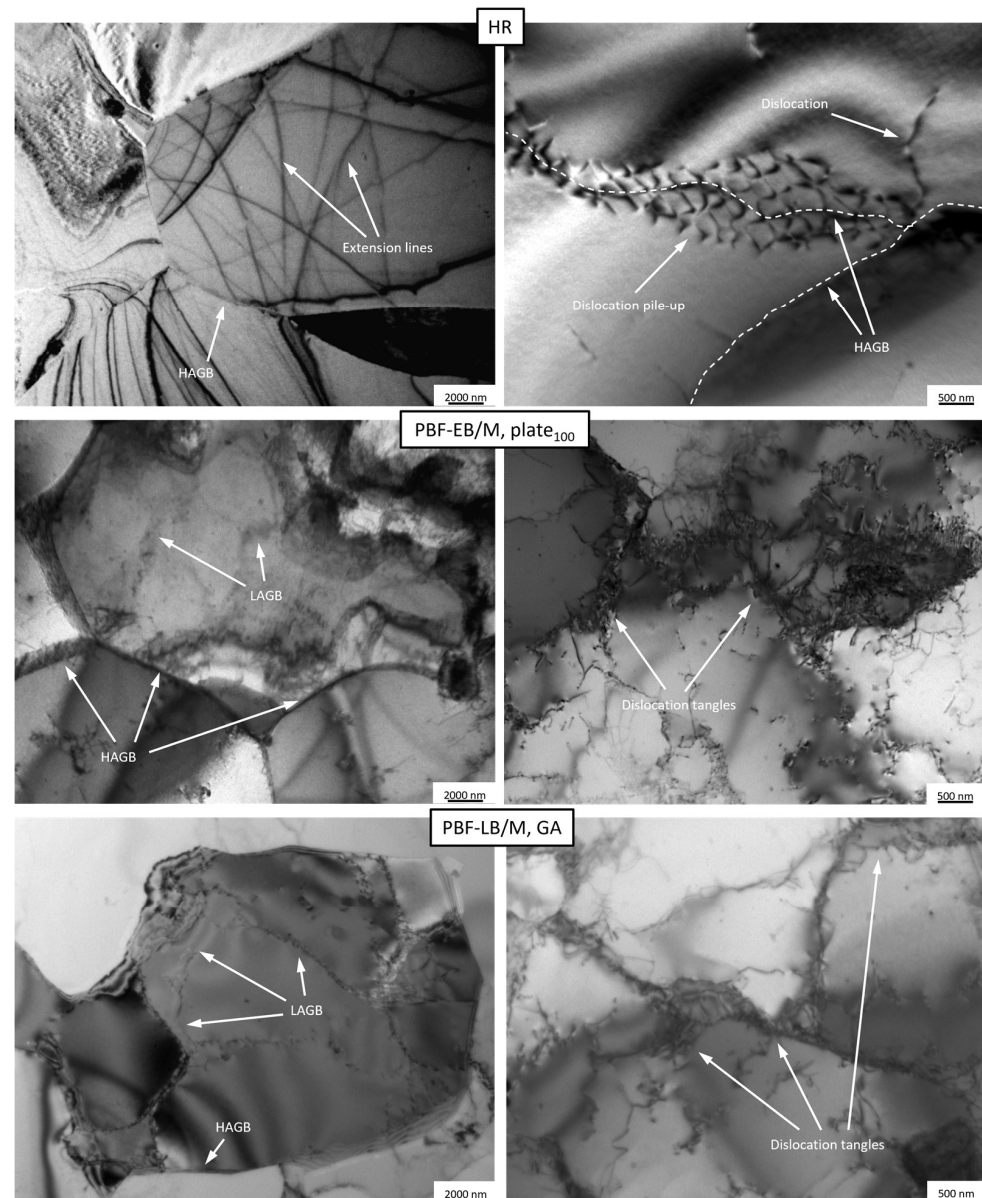


Figure 10. TEM images of the three characteristic conditions of Fe in focus: HR; PBF-EB/M, plate₁₀₀; and PBF-LB/M, GA; all tested up to nominal 10.25% strain. In the HR-Fe, dislocation pile-ups at a grain boundary (white dotted lines) can be seen, furthermore singular dislocations are visible (triangles). In the PBF-EB/M, plate₁₀₀ Fe as well as the PBF-LB/M, GA Fe, dislocation tangles of different sizes and densities are obvious. Note that the determination of the misorientation is not trivial via TEM, thus only a qualitative analysis of LAGBs and HAGBs is conducted.

For the HR specimen, dislocation pile-ups in the direct vicinity of HAGBs resulting from tensile deformation are confirmed. Since the HAGBs are strong obstacles for dislocation motion, dislocation pile-ups can be formed in the vicinity of the HAGBs [48]. Therefore, a very “classical” way of stress accommodation is found, since HAGBs are the only significant obstacles for deformation in the HR Fe and geometrically necessary dislocations emerge here. On the other side, in the PBF-LB/M, GA, as well as the PBF-EB/M, plate₁₀₀ Fe specimens, the presence of LAGBs inside the grains is evident. At higher magnifications, dislocation tangles (DT) become visible at LAGBs, indicating that process-induced LAGBs can hamper dislocation motion. A complex interaction of dislocations with LAGBs was reported to result in a strong resistance against the incident dislocation penetration [49]. Hence, the presence of LAGBs and their interaction with mobile dislocations can increase the strength of the material.

Figure 11 schematically depicts the mechanisms of stress accommodation in two characteristic microstructures, designated as “HR-type” and “non-recrystallized”. HR-type structures are dominated by HAGBs and a very low density of additional barriers (i.e., impurities, DTs, LAGBs, etc.) inside the grains and shall be representative for the HR-Fe as well as for the PBF-EB/M, plate₅₀ Fe. On the lower row, an idealized, non-recrystallized material condition is shown, characterized by pre-existing substructures formed by LAGBs as well as DTs. Despite showing different grain sizes (cf. Table 3) and residual stress states, both the PBF-LB/M manufactured and the PBF-EB/M, plate₁₀₀ Fe can be assigned to this type. Upon tensile deformation, dislocation multiplication and motion are expected in any case. TEM studies revealed that dislocation pile-ups are located at HAGBs. Is there no significant barrier within the matrix, dislocations might move freely through the grains and only pile up at the HAGBs. This is seen in HR-type conditions, where these sites eventually act as stress risers. In contrast, dislocations are effectively slowed down by LAGBs and entangle here in the non-recrystallized type. In the latter case, stresses are thought not to be as concentrated as in HR-type microstructures.

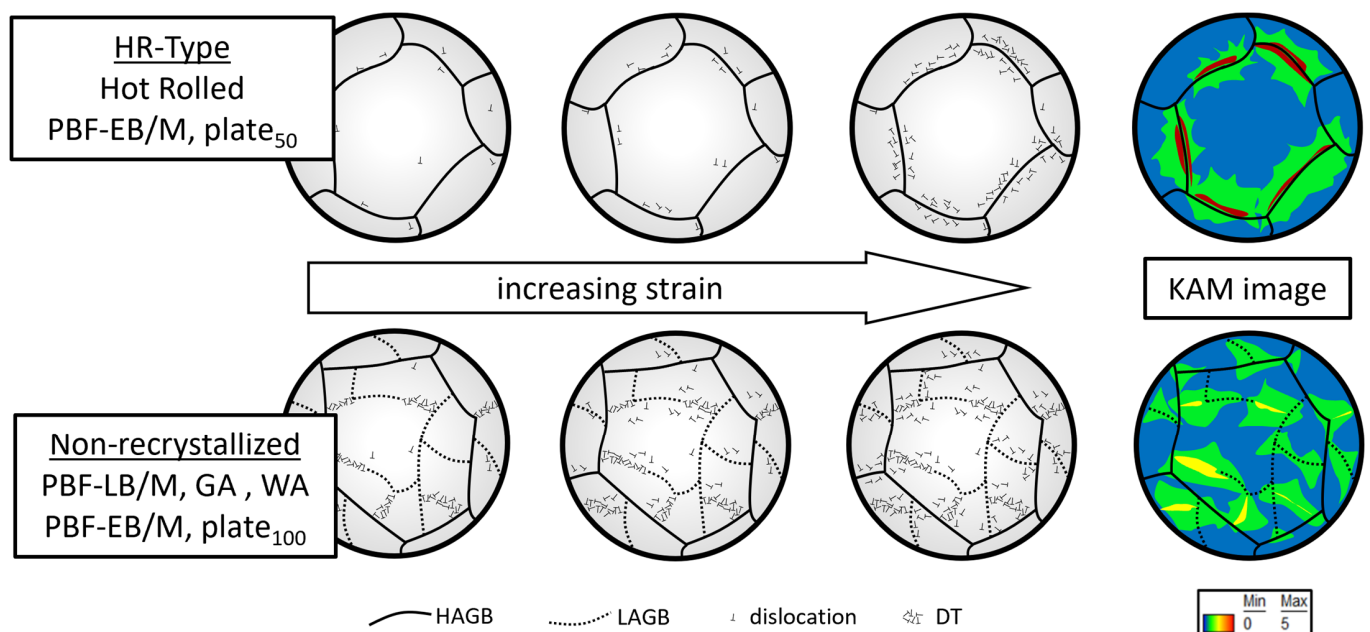


Figure 11. Schematic highlighting the evolution and accommodation of strain in the two characteristic microstructures. In the HR-type microstructure, dislocations accumulate at grain boundaries, eventually leading to stress concentrations. The non-recrystallized material condition is dominated by process induced LAGBs and DTs, which act as weak barriers and help to distribute the strain within the grains. At increasing strains, even more LAGBs can be formed by an accumulation of dislocations at DTs and increasing mismatch between two sub grains.

Highly dependent on the actual process conditions and, eventually, the specific thermal history, PB-AM manufactured parts experience rapid solidification and a high number of reheating cycles. The formation of subgrains and the increase in dislocation density is therefore possible, finally leading to very different as-built microstructures. As shown schematically in the model and experimentally by TEM analysis, dislocation movement during deformation can be affected in non-recrystallized specimens by the presence of LAGBs. Both HAGBs and LAGBs were previously found to be influential in order to strengthen PB-AM parts [20,50,51]. Furthermore, these dislocations can combine to form new substructures in the material upon deformation. The deformation-induced formation of new subgrains, considering Schmidt factors in each grain, requires further in-depth investigations beyond the scope of the present work.

In the presented work, five different cp-Fe microstructures are compared in as-built condition, after nominal 10.25% strain, and after failure. After assessment of the presented results, the following conclusion can be drawn: Hall-Petch is the predominant strengthening mechanism. This can be clearly deduced from the grain sizes displayed in Table 3, which obviously match the order of YS (Figure 7). In addition to the HAGB density, the presence of substructures within the grains must be considered. As can be seen from the IPF and KAM maps as well as the TEM images after applying a strain of 10.25%, the interaction of moving dislocations with obstacles in the matrix is complex. In HR-type microstructures, i.e., HR and PBF-EB/M, plate₅₀, no significant obstacles are present within a grain, and dislocations easily migrate through. This is reflected by the KAM maps (Figure 6) and the observation of pile-ups at HAGBs (Figure 10). In contrast, non-recrystallized material conditions are characterized by the presence of multiple barriers within the grains. From an experimental perspective, the differentiation of mosaicity, DTs, LAGBs, and HAGBs remains challenging and a matter of local lattice mismatch as well as the thickness and density of dislocation arrangements [52,53]. Their behavior upon plastic deformation has already been studied for different materials [20,21,34,54,55]. In the non-recrystallized material assessed in the present work, mosaicity further evolves in the grains upon plastic deformation. Here, the KAM maps indicate that dislocations accumulate in the vicinity of LAGBs after applying strain. TEM analysis points to the presence of a high density of DTs. In materials being characterized by facilitated cross slip, as is the case for cp-Fe, the formation of DTs and further LAGBs can occur [46]. Eventually, in cases of intense dislocation motion at higher strains, barriers that initially require low energy to be overcome by dislocations can consolidate, evolving into grain boundaries of low misorientation angle, and finally resulting in HAGBs at the highest deformations (if localized cracking does not set in earlier). At the highest strains and adequate stress states, this culminates in the mechanism known from SPD processes [56].

In the material conditions in focus, no phase boundaries or precipitates hinder dislocations from moving through the matrix. Their motion is hampered solely by HAGBs, LAGBs, and DTs, where the latter are barriers requiring relatively low energy to be overcome. Approaches can be found in literature, where the strengthening contributions are divided into a Hall-Petch and a work hardening component in dependence of the misorientation angle of the barrier [57]. As known from studies focusing on UFG materials, small grain sizes have a high potential for strengthening; however, they might bear the drawback of stress concentration at grain boundaries after a certain strain is applied [58]. This fact could be revealed in the present work in the case of the HR and PBF-EB/M, plate₅₀ specimens. On the contrary, low-energy obstacles like DTs and LAGBs can distribute stress more homogeneously inside the matrix and decelerate stress concentration under quasistatic loading conditions [46,59]. In consequence, very low strain hardening can be found. Finally, a microstructure dominated by finer grains, which in turn is characterized by a high fraction of sub-grain structures, can provide for a high strength and damage tolerance in cp-Fe as well as in low alloyed steels. Thus, an even higher strength could be achieved for the PBF-LB/M processed cp-Fe specimens. The potential of direct microstructure design is explicitly provided by PB-AM technologies. Still, the material behavior and microstructural

stability under complex loading conditions, e.g., fatigue and/or elevated temperature, must be addressed.

4. Conclusions

The present study provides an in-depth analysis of five different cp-Fe specimens with different microstructural and mechanical properties. By means of simple tensile tests accompanied by optical and electron microscopy as well as TEM analysis, the material conditions have been analyzed from the macroscale down to the nanoscale. From the investigations, two basically distinct types are distilled, which can be described as follows:

- “HR-type”, HAGB-dominated structures (HR; PBF-EB/M, plate₅₀ Fe) and
- “non-recrystallized” structures (PBF-LB/M, GA; PBF-LB/M, WA Fe; PBF-EB/M, plate₁₀₀ Fe)

These two distinct microstructures and their behavior are schematically illustrated in Figure 11. Their microstructural changes in the unloaded, partly strained, and finally failed specimen states and the deformation mechanisms leading to the material response of cp-Fe are investigated and can be summarized as follows:

- The Hall-Petch relation was found to be the predominant strengthening mechanism, as the fine-grained PBF-LB/M specimens exhibited the highest strength among the examined conditions.
- In the HAGB-dominated conditions, i.e., the HR and the PBF-EB/M, plate₅₀ specimens, plastic strain leads to dislocation pile-ups at grain boundaries, eventually leading to severe stress concentrations.
- In LAGB-dominated material conditions, DTs and LAGBs are soft barriers for dislocations resulting in a rather homogeneous strain distribution, and, hence, high damage tolerance and ductility. With increasing deformation, dislocations were detected in the direct vicinity of LAGBs and also a high number of DTs. These findings could be confirmed by TEM analysis.

It is shown that a fine-grained microstructure governed by HAGBs can provide high strength but bears the disadvantage of stress concentration, whereas DTs and LAGBs can contribute to a stress distribution within the microstructure. Thus, combining microstructures, i.e., low grain sizes but high fractions of LAGBs, can allow for higher strengths and damage tolerance.

Author Contributions: Conceptualization, C.J.J.T. and S.V.S.; Methodology, G.G.; Investigation, C.J.J.T. and G.G.; Writing—original draft, C.J.J.T.; Writing—review & editing, C.J.J.T., S.V.S., J.R. and T.N.; Visualization, C.J.J.T., S.V.S. and J.R.; Supervision, T.N.; Funding acquisition, T.N. All authors have read and agreed to the published version of the manuscript.

Funding: This work was supported by the Deutsche Forschungsgemeinschaft (DFG) under Grant number 413259151.

Data Availability Statement: The raw data supporting the conclusions of this article will be made available by the authors on request.

Conflicts of Interest: The authors declare no conflict of interest.

References

1. DebRoy, T.; Wei, H.L.; Zuback, J.S.; Mukherjee, T.; Elmer, J.W.; Milewski, J.O.; Beese, A.M.; Wilson-Heid, A.D.; De, A.; Zhang, W. Additive manufacturing of metallic components—Process, structure and properties. *Prog. Mater. Sci.* **2018**, *92*, 112–224. [[CrossRef](#)]
2. Cordero, Z.C.; Meyer, H.M.; Nandwana, P.; Dehoff, R.R. Powder bed charging during electron-beam additive manufacturing. *Acta Mater.* **2017**, *124*, 437–445. [[CrossRef](#)]
3. Körner, C. Additive manufacturing of metallic components by selective electron beam melting—A review. *Int. Mater. Rev.* **2016**, *61*, 361–377. [[CrossRef](#)]
4. Song, B.; Dong, S.; Deng, S.; Liao, H.; Coddet, C. Microstructure and tensile properties of iron parts fabricated by selective laser melting. *Opt. Laser Technol.* **2014**, *56*, 451–460. [[CrossRef](#)]

5. Song, B.; Dong, S.; Liu, Q.; Liao, H.; Coddet, C. Vacuum heat treatment of iron parts produced by selective laser melting: Microstructure, residual stress and tensile behavior. *Mater. Des.* **2014**, *54*, 727–733. [[CrossRef](#)]
6. Dehoff, R.R.; Kirka, M.M.; Sames, W.J.; Bilheux, H.; Tremsin, A.S.; Lowe, L.E.; Babu, S.S. Site specific control of crystallographic grain orientation through electron beam additive manufacturing. *Mater. Sci. Technol.* **2015**, *31*, 931–938. [[CrossRef](#)]
7. Helmer, H.; Bauereiß, A.; Singer, R.; Körner, C. Grain structure evolution in Inconel 718 during selective electron beam melting. *Mater. Sci. Eng. A* **2016**, *668*, 180–187. [[CrossRef](#)]
8. Raghavan, N.; Dehoff, R.; Pannala, S.; Simunovic, S.; Kirka, M.; Turner, J.; Carlson, N.; Babu, S.S. Numerical modeling of heat-transfer and the influence of process parameters on tailoring the grain morphology of IN718 in electron beam additive manufacturing. *Acta Mater.* **2016**, *112*, 303–314. [[CrossRef](#)]
9. Ding, X.; Koizumi, Y.; Aoyagi, K.; Kii, T.; Sasaki, N.; Hayasaka, Y.; Yamanaka, K.; Chiba, A. Microstructural control of alloy 718 fabricated by electron beam melting with expanded processing window by adaptive offset method. *Mater. Sci. Eng. A* **2019**, *764*, 138058. [[CrossRef](#)]
10. Karimi, P.; Sadeghi, E.; Ålgårdh, J.; Olsson, J.; Colliander, M.H.; Harlin, P.; Toyserkani, E.; Andersson, J. Tailored grain morphology via a unique melting strategy in electron beam-powder bed fusion. *Mater. Sci. Eng. A* **2021**, *824*, 141820. [[CrossRef](#)]
11. Scharowsky, T.; Bauereiß, A.; Körner, C. Influence of the hatching strategy on consolidation during selective electron beam melting of Ti-6Al-4V. *Int. J. Adv. Manuf. Technol.* **2017**, *92*, 2809–2818. [[CrossRef](#)]
12. Niendorf, T.; Brenne, F.; Schaper, M.; Riemer, A.; Leuders, S.; Reimche, W.; Schwarze, D.; Maier, H.J. Labelling additively manufactured parts by microstructural gradation—Advanced copy-proof design. *Rapid Prototyp. J.* **2016**, *22*, 630–635. [[CrossRef](#)]
13. Damon, J.; Koch, R.; Kaiser, D.; Graf, G.; Dietrich, S.; Schulze, V. Process development and impact of intrinsic heat treatment on the mechanical performance of selective laser melted AISI 4140. *Addit. Manuf.* **2019**, *28*, 275–284. [[CrossRef](#)]
14. Hearn, W.; Steinlechner, R.; Hryha, E. Laser-based powder bed fusion of non-weldable low-alloy steels. *Powder Metall.* **2021**, *173*, 121–132. [[CrossRef](#)]
15. Kürnsteiner, P.; Wilms, M.B.; Weisheit, A.; Gault, B.; Jägler, E.A.; Raabe, D. High-strength Damascus steel by additive manufacturing. *Nature* **2020**, *582*, 515–519. [[CrossRef](#)] [[PubMed](#)]
16. Günther, J.; Brenne, F.; Droste, M.; Wendler, M.; Volkova, O.; Biermann, H.; Niendorf, T. Design of novel materials for additive manufacturing—Isotropic microstructure and high defect tolerance. *Sci. Rep.* **2018**, *8*, 1298. [[CrossRef](#)]
17. Lejček, P.; Čapek, J.; Roudnická, M.; Molnárová, O.; Maňák, J.; Duchoň, J.; Dvorský, D.; Koller, M.; Seiner, H.; Svora, P.; et al. Selective laser melting of iron: Multiscale characterization of mechanical properties. *Mater. Sci. Eng. A* **2021**, *800*, 140316. [[CrossRef](#)]
18. Lejček, P.; Roudnická, M.; Čapek, J.; Dvorský, D.; Drahoukoupil, J.; Šimek, D.; Čížek, J.; Svora, P.; Molnárová, O.; Vojtěch, D. Selective laser melting of pure iron: Multiscale characterization of hierarchical microstructure. *Mater. Charact.* **2019**, *154*, 222–232. [[CrossRef](#)]
19. Eskandari Sabzi, H.; Rivera-Díaz-del-Castillo, P.E. Composition and process parameter dependence of yield strength in laser powder bed fusion alloys. *Mater. Des.* **2020**, *195*, 109024. [[CrossRef](#)]
20. Sabzi, H.E.; Hernandez-Nava, E.; Li, X.-H.; Fu, H.; San-Martín, D.; Rivera-Díaz-Del-Castillo, P.E. Strengthening control in laser powder bed fusion of austenitic stainless steels via grain boundary engineering. *Mater. Des.* **2021**, *212*, 110246. [[CrossRef](#)]
21. Liu, L.; Ding, Q.; Zhong, Y.; Zou, J.; Wu, J.; Chiu, Y.-L.; Li, J.; Zhang, Z.; Yu, Q.; Shen, Z. Dislocation network in additive manufactured steel breaks strength–ductility trade-off. *Mater. Today* **2018**, *21*, 354–361. [[CrossRef](#)]
22. Cooman BC de Kwon, O.; Chin, K.-G. State-of-the-knowledge on TWIP steel. *Mater. Sci. Technol.* **2012**, *28*, 513–527. [[CrossRef](#)]
23. Cooman BC de Estrin, Y.; Kim, S.K. Twinning-induced plasticity (TWIP) steels. *Acta Mater.* **2018**, *142*, 283–362. [[CrossRef](#)]
24. Droste, M.; Günther, J.; Kotzem, D.; Walther, F.; Niendorf, T.; Biermann, H. Cyclic deformation behavior of a damage tolerant CrMnNi TRIP steel produced by electron beam melting. *Int. J. Fatigue* **2018**, *114*, 262–271. [[CrossRef](#)]
25. George, E.P.; Raabe, D.; Ritchie, R.O. High-entropy alloys. *Nat. Rev. Mater.* **2019**, *4*, 515–534. [[CrossRef](#)]
26. Huang, Y.; Langdon, T.G. Advances in ultrafine-grained materials. *Mater. Today* **2013**, *16*, 85–93. [[CrossRef](#)]
27. Richter, J.; Torrent, C.J.J.; Krochmal, M.; Wegener, T.; Vollmer, M.; Niendorf, T. A comparative study using water atomized and gas atomized powder in laser powder bed fusion—Assessment of the fatigue performance. *Int. J. Fatigue* **2023**, *168*, 107468. [[CrossRef](#)]
28. Richter, J.; Wegener, T.; Kratzsch, R.; Vollmer, M.; Peuker, U.; Niendorf, T. On the structural integrity and fatigue performance of additively manufactured Ti-6Al-4V parts processed using mechanically recycled powders. *Int. J. Fatigue* **2023**, *176*, 107903. [[CrossRef](#)]
29. Torrent, C.; Krooß, P.; Niendorf, T. On the Impact of Build Envelope Sizes on E-PBF Processed Pure Iron. *Metall. Mater. Trans. B* **2021**, *53*, 8–13. [[CrossRef](#)]
30. Torrent, C.; Wackenrohr, S.; Richter, J.; Sobrero, C.E.; Degener, S.; Krooß, P.; Maier, H.J.; Niendorf, T. On the microstructural and cyclic mechanical properties of pure iron processed by electron beam melting. *Adv. Eng. Mater.* **2021**, *23*, 2100018. [[CrossRef](#)]
31. Torrent, C.J.J.; Krooß, P.; Huang, J.; Voigt, M.; Ebbert, C.; Knust, S.; Grundmeier, G.; Niendorf, T. Oxide Modified Iron in Electron Beam Powder Bed Fusion—From Processability to Corrosion Properties. *Alloys* **2022**, *1*, 31–53. [[CrossRef](#)]
32. Wackenrohr, S.; Torrent, C.J.J.; Herbst, S.; Nürnberger, F.; Krooß, P.; Ebbert, C.; Voigt, M.; Grundmeier, G.; Niendorf, T.; Maier, H.J. Corrosion fatigue behavior of electron beam melted iron in simulated body fluid. *npj Mater. Degrad.* **2022**, *6*, 18. [[CrossRef](#)]
33. Oliveira, J.P.; LaLonde, A.D.; Ma, J. Processing parameters in laser powder bed fusion metal additive manufacturing. *Mater. Des.* **2020**, *193*, 108762. [[CrossRef](#)]

34. Picak, S.; Wegener, T.; Sajadifar, S.; Sobrero, C.; Richter, J.; Kim, H.; Niendorf, T.; Karaman, I. On the low-cycle fatigue response of CoCrNiFeMn high entropy alloy with ultra-fine grain structure. *Acta Mater.* **2021**, *205*, 116540. [[CrossRef](#)]
35. Frank, F.C.; Read, W.T. Multiplication Processes for Slow Moving Dislocations. *Phys. Rev.* **1950**, *79*, 722–723. [[CrossRef](#)]
36. Frank, F.C. The Frank—Read source. *Proc. R. Soc. Lond. A Math. Phys. Sci.* **1980**, *371*, 136–138.
37. Fan, H.; Aubry, S.; Arsenlis, A.; El-Awady, J.A. The role of twinning deformation on the hardening response of polycrystalline magnesium from discrete dislocation dynamics simulations. *Acta Mater.* **2015**, *92*, 126–139. [[CrossRef](#)]
38. Bartlett, J.L.; Li, X. An overview of residual stresses in metal powder bed fusion. *Addit. Manuf.* **2019**, *27*, 131–149. [[CrossRef](#)]
39. Sochalski-Kolbus, L.M.; Payzant, E.A.; Cornwell, P.A.; Watkins, T.R.; Babu, S.S.; Dehoff, R.R.; Lorenz, M.; Ovchinnikova, O.; Duty, C. Comparison of Residual Stresses in Inconel 718 Simple Parts Made by Electron Beam Melting and Direct Laser Metal Sintering. *Metall. Mat. Trans. A* **2015**, *46*, 1419–1432. [[CrossRef](#)]
40. Javaid, F.; Pouriayevali, H.; Durst, K. Dislocation–grain boundary interactions: Recent advances on the underlying mechanisms studied via nanoindentation testing. *J. Mater. Res.* **2021**, *36*, 2545–2557.
41. Li, Y.; Lietaert, K.; Li, W.; Zhang, X.-Y.; Leeftang, M.A.; Zhou, J.; Zadpoor, A.A. Corrosion fatigue behavior of additively manufactured biodegradable porous iron. *Corros. Sci.* **2019**, *156*, 106–116. [[CrossRef](#)]
42. Bertsch, K.; de Bellefon, G.M.; Kuehl, B.; Thoma, D. Origin of dislocation structures in an additively manufactured austenitic stainless steel, 3.1.6.L. *Acta Mater.* **2020**, *199*, 19–33. [[CrossRef](#)]
43. Lindroos, M.; Pinomaa, T.; Ammar, K.; Laukkanen, A.; Provatas, N.; Forest, S. Dislocation density in cellular rapid solidification using phase field modeling and crystal plasticity. *Int. J. Plast.* **2022**, *148*, 103139. [[CrossRef](#)]
44. Bruder, E. Mechanical Properties of ARMCO[®] Iron after Large and Severe Plastic Deformation—Application Potential for Precursors to Ultrafine Grained Microstructures. *Metals* **2018**, *8*, 191. [[CrossRef](#)]
45. Wang, Y.B.; Li, B.Q.; Sui, M.L.; Mao, S.X. Deformation-induced grain rotation and growth in nanocrystalline Ni. *Appl. Phys. Lett.* **2008**, *92*, 11903. [[CrossRef](#)]
46. Dhal, A.; Panigrahi, S.K.; Shunmugam, M.S. Achieving excellent microformability in aluminum by engineering a unique ultrafine-grained microstructure. *Sci. Rep.* **2019**, *9*, 10683. [[CrossRef](#)]
47. Hutanu, R.; Clapham, L.; Rogge, R.B. Intergranular strain and texture in steel Luders bands. *Acta Mater.* **2005**, *53*, 3517–3524. [[CrossRef](#)]
48. Pan, H.; He, Y.; Zhang, X. Interactions between Dislocations and Boundaries during Deformation. *Materials* **2021**, *14*, 1012. [[CrossRef](#)]
49. Liu, B.; Raabe, D.; Eisenlohr, P.; Roters, F.; Arsenlis, A.; Hommes, G. Dislocation interactions and low-angle grain boundary strengthening. *Acta Mater.* **2011**, *59*, 7125–7134. [[CrossRef](#)]
50. Abdi, F.; Eftekharian, A.; Huang, D.; Rebak, R.B.; Rahmane, M.; Sundararaghavan, V.; Kanyuck, A.; Gupta, S.K.; Arul, S.; Jain, V.; et al. Grain boundary engineering of new additive manufactured polycrystalline alloys. *Forces Mech.* **2021**, *4*, 100033. [[CrossRef](#)]
51. Haghdad, N.; Laleh, M.; Moyle, M.; Primig, S. Additive manufacturing of steels: A review of achievements and challenges. *J. Mater. Sci.* **2021**, *56*, 64–107. [[CrossRef](#)]
52. Muñoz, J.A.; Bolmaro, R.E.; Jorge, A.M.; Zhilyaev, A.; Cabrera, J.M. Prediction of Generation of High- and Low-Angle Grain Boundaries (HAGB and LAGB) During Severe Plastic Deformation. *Metall. Mater. Trans. A* **2020**, *51*, 4674–4684. [[CrossRef](#)]
53. Muñoz, J.A.; Higuera, O.F.; Benito, J.A.; Bradai, D.; Khelfa, T.; Bolmaro, R.E.; Jorge, A.M.; Cabrera, J.M. Analysis of the micro and substructural evolution during severe plastic deformation of ARMCO iron and consequences in mechanical properties. *Mater. Sci. Eng. A* **2019**, *740–741*, 108–120. [[CrossRef](#)]
54. Zhu, Z.; Li, W.; Nguyen, Q.B.; An, X.; Lu, W.; Li, Z.; Ng, F.L.; Nai, S.M.L.; Wei, J. Enhanced strength–ductility synergy and transformation-induced plasticity of the selective laser melting fabricated 304L stainless steel. *Addit. Manuf.* **2020**, *35*, 101300. [[CrossRef](#)]
55. Wang, Y.M.; Voisin, T.; McKeown, J.T.; Ye, J.; Calta, N.P.; Li, Z.; Zeng, Z.; Zhang, Y.; Chen, W.; Roehling, T.T.; et al. Additively manufactured hierarchical stainless steels with high strength and ductility. *Nat. Mater.* **2018**, *17*, 63–71. [[CrossRef](#)]
56. Estrin, Y.; Vinogradov, A. Extreme grain refinement by severe plastic deformation: A wealth of challenging science. *Acta Mater.* **2013**, *61*, 782–817. [[CrossRef](#)]
57. Hansen, N. Hall–Petch relation and boundary strengthening. *Scr. Mater.* **2004**, *51*, 801–806. [[CrossRef](#)]
58. Niendorf, T.; Canadinc, D.; Maier, H.J. Fatigue Damage Evolution in Ultrafine-Grained Interstitial-Free Steel. *Adv. Eng. Mater.* **2011**, *13*, 275–280. [[CrossRef](#)]
59. Ma, Y.; Yang, M.; Jiang, P.; Yuan, F.; Wu, X. Plastic deformation mechanisms in a severely deformed Fe-Ni-Al-C alloy with superior tensile properties. *Sci. Rep.* **2017**, *7*, 15619. [[CrossRef](#)]

Disclaimer/Publisher’s Note: The statements, opinions and data contained in all publications are solely those of the individual author(s) and contributor(s) and not of MDPI and/or the editor(s). MDPI and/or the editor(s) disclaim responsibility for any injury to people or property resulting from any ideas, methods, instructions or products referred to in the content.